Surface & Coatings Technology 513 (2025) 132498

Contents lists available at ScienceDirect

Surface & Coatings Technology

journal homepage: www.elsevier.com/locate/surfcoat

Thermal conductivity and micromechanical properties of plasma-sprayed yttria-stabilized zirconia thermal barrier coatings

Stefania Morelli [a,*], Simone Bursich [b], Giovanni Bolelli [a,c,d], Pietro Puddu [e], Edoardo Rossi [f], Francesco Gerardo Mecca [a], Luca Bortolotti [a], Luca Lusvarghi [a,c,d]

[a] Department of Engineering "Enzo Ferrari", Università di Modena e Reggio Emilia, Via Pietro Vivarelli 10/1, 41125 Modena (MO), Italy
[b] Lincotek Rubbiano S.p.A., Via Mistrali 7, 43046 Rubbiano di Solignano, (PR), Italy
[c] InterMech – MO.RE. Centro Interdipartimentale per la Ricerca Applicata e i Servizi nel Settore della Meccanica Avanzata e della Motoristica, Università di Modena e Reggio Emilia, Via Pietro Vivarelli 2, 41125 Modena (MO), Italy
[d] Consorzio Interuniversitario Nazionale per la Scienza e Tecnologia dei Materiali (INSTM), Local Unit: Università di Modena e Reggio Emilia, Via Pietro Vivarelli 10/1, 41125 Modena (MO), Italy
[e] Il Sentiero International Campus S.r.l., 36015 Schio (VI), Italy
[f] Department of Civil, Computer Science and Aeronautical Technologies Engineering, Università di Roma 3, Via Vito Volterra 62, 00146 Roma, Italy

ARTICLE INFO

Keywords:
Thermal barrier coating (TBC)
Yttria stabilized zirconia (YSZ)
Powder manufacturing
Thermal conductivity
Fracture toughness
Pillar splitting

ABSTRACT

Plasma-sprayed ZrO_2 – 8 wt% Y_2O_3 (8YSZ) is the most widely used kind of thermal barrier coating (TBC) to insulate components in the hot gas path of industrial gas turbines. The thermal conductivity of an 8YSZ TBC depends on its microstructure, which is influenced by the characteristics of the feedstock powder. Thus, in this paper, we studied the thermal conductivity of 8YSZ coatings deposited using agglomerated and sintered (A&S), fused and crushed (F&C) and hollow spherical (HOSP) feedstock powders, both in the as-deposited condition and after thermal cycling. The coating from the A&S powder, which exhibited greater porosity (≈22 %), also had lower thermal conductivity in as-deposited condition (0.54 W/(m·K)) compared to the coatings from F&C (0.89 W/(m·K)) and HOSP (0.70 W/(m·K)) powders. Its thermal conductivity also increased less than that of the other coatings after thermal cycling.

Because ZrO_2 with a higher Y_2O_3 content is attracting interest as the top layer of molten silicate-resistant TBCs, we also studied the thermal conductivity of bilayer systems with an 8YSZ bottom layer and a top layer of ZrO_2 – 20 wt% Y_2O_3 (20YSZ) or ZrO_2 – 55 wt% Y_2O_3 (55YSZ), all obtained from an A&S feedstock. We found comparable thermal conductivities of ≈0.5–0.6 W/(m•K) and, again, a tendency to increase slightly after thermal cycling.

Furthermore, because 20YSZ and 55YSZ are fully stabilized in the cubic form, therefore potentially more brittle than 8YSZ, we also measured the intrinsic indentation fracture toughness of these materials by pillar splitting. Both 20YSZ and 55YSZ had a similar toughness of 1.39 MPa$\sqrt{m}$, compared to 2.32 MPa$\sqrt{m}$ for 8YSZ.

1. Introduction

In applications involving extreme heat, effective thermal insulation is crucial for metallic components. Here, thermal barrier coatings (TBCs) come into play. TBCs are specially designed ceramic coatings that act as thermal insulators for metallic components that operate in contact with gas flows at temperatures that can reach 1600 °C. By providing a protective layer, TBCs help minimise heat transfer, preserving the integrity and performance of critical components across various industries. A key requirement for TBCs is having low thermal conductivity.

There are several strategies to achieve low thermal conductivity. One approach involves carefully selecting materials, such as Yttria Stabilized Zirconia (YSZ), which exhibits a thermal conductivity of 2.3 W/(m•K) at 1000 °C (bulk value) [1]. The low thermal conductivity of YSZ is attributed to the high concentration of point defects, including oxygen vacancies and substitutional solute atoms. These defects effectively scatter heat-conducting phonons, which are lattice waves responsible for thermal conduction.

In fact, increasing the yttria content in YSZ coatings causes a progressive decrease in their thermal conductivity. For instance, Hasselman

---

* Corresponding author.
E-mail address: stefania.morelli@unimore.it (S. Morelli).

https://doi.org/10.1016/j.surfcoat.2025.132498
Received 19 February 2025; Received in revised form 9 June 2025; Accepted 15 July 2025

et al. carried out experiments involving YSZ coatings with varying levels of yttria [1]. Their findings indicated that zirconia with high yttria content, possessing a cubic crystalline phase, demonstrated lower thermal conductivity compared to zirconia with a tetragonal crystalline phase and lower yttria content. This is corroborated by a study on bulk zirconia ceramics by Song et al. [2]. However, compared to the typical ZrO_2 + 7–8 wt% Y_2O_3 (8YSZ) composition, which features a non-transformable tetragonal (t') structure toughened by a ferroelastic mechanism [3], cubic ZrO_2 is more brittle [3,4]. Therefore, early spallation would occur when employed as a single-layer TBC [5], and, as we showed in our earlier work, it must be employed as the top layer in a TBC system with an 8YSZ underlying layer bearing the large stresses that occur at the interface with the metallic bond coat and its thermally grown oxide (TGO) scale [6].

Apart from the inherent properties of YSZ, another effective strategy to further reduce thermal conductivity is to introduce porosity within the coatings. When porosity is incorporated, the path of heat transfer is disrupted, resulting in a significant decrease in thermal conductivity. In particular, porous coatings created through the atmospheric plasma spraying deposition (APS) process have shown a reduction in thermal conductivity to <1 W/(m•K) [7,8]. Plasma-sprayed YSZ coatings also exhibit lower thermal conductivity compared to columnar coatings obtained by Electron Beam-Physical Vapor Deposition (EB-PVD), whose conductivity is reportedly around 1.6 W/(m•K) [9]. Previous studies established a strong correlation between porosity and thermal conductivity. Kulkarni et al. found that microstructural characteristics, specifically interlamellar pores, intersplat cracks, and globular pores, play an important role in determining the thermal conductivity of plasma-sprayed coatings [10]. YSZ thermal barrier coatings obtained using fused and crushed feedstock powders exhibited higher thermal conductivity due to their density, while coatings deposited through spherical sol-gel particles displayed lower thermal conductivity due to the numerous interlamellar pores. Coatings obtained from hollow spherical (HOSP) powders had the lowest thermal conductivity, mainly influenced by intersplat boundaries, despite their overall porosity being similar to that of agglomerated and sintered coatings. This was also confirmed by Chi and Sampath, who revealed that the use of HOSP powders led to as-sprayed coatings with more interlamellar pores and splat boundaries, which had a substantial effect in reducing thermal conductivity [11]. Markocsan et al. demonstrated that flat, longitudinally oriented pores lead to a more significant decrease in thermal conductivity compared to circular pores [12]. Huang et al. pointed out that the shape of the pores can also affect the thermal conductivity of TBCs [13]. Other studies investigated the relation between exposure to high temperatures and thermal conductivity [14,15]. Indeed, under prolonged high-temperature service conditions, the reduction of porosity caused by sintering affects thermal conductivity. The degree of porosity is not only influenced by the service temperature but also by its duration. For example, Kim et al. discovered that samples subjected to a heat treatment at 1200 °C for 175 h displayed higher thermal conductivity compared to those treated at 1250 °C for 100 h [16].

As the above review of the literature shows, the manufacturing route of the feedstock powder and, consequently, its microstructure have a major influence on the porosity and properties of the resulting plasma-sprayed TBCs. However, studies on this topic are still scarce, with [10,11] being among the few existing works. Moreover, those papers did not study the fracture toughness of the material, which, as mentioned above, is another key property for thermal barrier coatings. Indeed, TBCs must resist crack propagation under the stresses imposed by thermal cycling conditions. For example, Taylor et al. [4] showed a continuous decrease in fracture toughness in ZrO_2 when the amount of Y_2O_3 increased from 8 wt% to 10 wt% and 12 wt%. However, technologically interesting high-yttria compositions, corresponding to commercially available feedstock powders, currently feature a much higher Y_2O_3 content, because as a top layer this material has benefits in terms of improved resistance to corrosion by molten CaO – MgO – Al_2O_3 – SiO_2 (CMAS) deposits [17,18].

Therefore, following up on our previous work where we investigated the functional performance, i.e. thermal cycling resistance and CMAS corrosion resistance, of thermal barrier coatings obtained from different feedstock materials and with different yttria content, this paper addresses three main topics:

- Providing a comparative analysis of the thermal conductivity of 8YSZ coatings obtained using feedstock powders with different morphologies and subjected to different numbers of thermal fatigue cycles, to encompass the effects of sintering on thermal conductivity as well.
- Comparing the thermal conductivities of 8YSZ, ZrO_2 + 20 wt% Y_2O_3 (20YSZ), and ZrO_2 + 55 wt% Y_2O_3 (55YSZ) coatings, all deposited using feedstock powders obtained by the same manufacturing route, and all subjected to thermal cycling fatigue.
- Comparing the "intrinsic" mechanical properties of 8YSZ, ZrO_2 + 20 wt% Y_2O_3 (20YSZ), and ZrO_2 + 55 wt% Y_2O_3 (55YSZ) materials by performing small-scale tests using nano-indentation and pillar-splitting methods.

Concerning the latter point, information on the "intrinsic" mechanical properties of TBC materials is essential to understanding their response to crack propagation during thermal cycling, but their assessment is made difficult by the porosity of TBCs. Most of the literature works (including the data in [4]) report the results of macroscale tests where all results are affected by porosity. Alternatively, other works report values measured on bulk samples. However, their grain structure differs substantially from that of a plasma sprayed splat subjected to rapid quenching and directional solidification. In this work, we use high-speed nanoindentation to measure hardness and elastic modulus in small volumes of material [19,20], and the pillar splitting method to evaluate the indentation fracture toughness.

Pillar splitting [21–24] represents a novel alternative to traditional microindentation techniques [25]. This approach avoids the complications of measuring the lengths of the cracks, as it is done in conventional measurements of indentation fracture toughness by Vickers indentation. It also reduces the effects of residual stresses, which are alleviated as the pillar separates from the surrounding material during focused ion beam (FIB) milling [26], and is less sensitive to pores and defects, although it is not possible to exclude that some defects might still exist in the small volume of FIB-machined pillars. This method has been implemented across a range of materials, including silicon [21], ceramic films such as TiN and CrN [21,27], composite coatings such as CrAlN/Si_3N_4 [24], as well as thermally sprayed YSZ coatings [28,29].

2. Materials and methods

2.1. Feedstock materials and coating deposition

Agglomerated and Sintered (A&S), Hollow Spherical (HOSP), and Fused and Crushed (F&C) powders were used to produce three porous 7-8YSZ monolayers (Table 1) by atmospheric plasma spraying (APS).

Additionally, two bi-layer coating systems were also deposited by APS. The bottom layer consisted of 7-8YSZ, while the top layer consisted of porous 20YSZ and 55YSZ, respectively. In this case, the 20YSZ and 55YSZ layers were deposited using agglomerated and sintered powders (Table 1). It was not possible to perform an analogous study of the effect of the powder manufacturing route on the properties of these two layers because fused and crushed and HOSP powders are not commercially available for these compositions.

A cascaded plasma torch from Lincotek Equipment S.p.A. was employed to apply the ceramic coatings at Lincotek Rubbiano S.p.A. under industrial processing conditions. The substrates used were Hastelloy-X coupons with a thickness of 3 mm and a diameter of 25.4 mm. These coupons underwent a preliminary deposition of a 200 μm-

Table 1
List of feedstock materials employed in this work.

Sample ID	Composition bottom layer	Composition top layer	Powder manufacturing process	Particle size distribution: d_{10} / d_{50} / d_{90} [μm]
AP	ZrO_2–8 wt% Y_2O_3	–	Agglomerated and sintered	23/55/94
FP	ZrO_2–8 wt% Y_2O_3	–	Fused and crushed	37/65/105
HP	ZrO_2–8 wt% Y_2O_3	–	HOSP	21/53/86
20AP	ZrO_2–8 wt% Y_2O_3	ZrO_2–20 wt% Y_2O_3	Agglomerated and sintered	15/50/95
55AP	ZrO_2–8 wt% Y_2O_3	ZrO_2–55 wt% Y_2O_3	Agglomerated and sintered	19/40/72

thick NiCoCrAlY bond coat (Höganäs Amperit 415) using the High-Velocity Oxygen-Fuel (HVOF)-APS "flash" method. After application of the bond coat, a vacuum heat treatment was performed at approximately 1100 °C for a duration of 2 h, as per the standard industrial production practice.

2.2. Microstructural characterization and phase composition

The samples were cold mounted in epoxy resin and cut using a resin-bound Al_2O_3 abrasive disc. The resulting cross-sections were then ground using SiC papers and polished using a polycrystalline diamond suspension and an oxide polishing suspension (OPS) for microstructural analysis. The same cold-mounting, grinding, and polishing procedures were applied to analyse the cross-sections of the feedstock powders.

All samples were observed with a scanning electron microscope (SEM: Quanta-200, FEI - ThermoFisher Scientific, Eindhoven, NL) equipped with an INCA energy-dispersive X-ray (EDX) detector (INCA, Oxford Instruments Analytical, Oxford, UK) for qualitative and semi-quantitative chemical analysis. SEM micrographs and EDX spectra were obtained with a 25 keV electron beam energy. To ensure electrical conductivity, the samples were sputter-coated with a layer of Au. Furthermore, detailed SEM micrographs were acquired using a Nova NanoSEM 450 (FEI - ThermoFisher Scientific) equipped with a field emission gun (FEG) source and a Quantax-200 EDX system (Bruker Nano GmbH, Berlin, Germany) with an Xflash-6|10 detector. Detailed micrographs exploiting the electron channelling contrast were captured at a low electron beam energy of 3 keV on samples without the sputtered Au layer.

SEM micrographs with a magnification of 1000× were acquired to assess the porosity of the coatings. For each sample, six images were captured from various areas and subsequently analysed using image analysis software (ImageJ – NIH, Bethesda, Maryland, USA) to convert the greyscale images into binary black and white images to measure the percentage of area occupied by voids. Specifically, in addition to the total porosity, the image analysis procedure allowed to differentiate between globular pores and microcracks by setting a circularity threshold. All objects with a circularity of 0.6 or less were considered to be cracks, while objects with circularity >0.6 were considered globular pores.

XRD patterns (X'Pert PRO diffractometer, Malvern Panalytical, Almelo, The Netherlands) were obtained on as-sprayed coatings using Cu-Kα radiation emitted from an X-ray tube operated at 40 mA, 40 kV and detected by a 1D array of solid-state detectors (X'Celerator, Malvern Panalytical). An angular range of $20^\circ \leq 2\theta \leq 85^\circ$ was scanned with a step of 0.0167° and a counting time of 120 s/step.

2.3. Thermal diffusivity and conductivity measurement

The main objective of this analysis was to determine the thermal diffusivity and conductivity values using laser flash analysis. The evaluation was carried out on the three monolayer coatings obtained from the different feedstock powders, namely AP, HP, and FP, as indicated in Table 1.

In addition, we also examined the thermal effects arising from the application of a top layer composed of 20YSZ or 55YSZ. In this work, we chose to evaluate the thermal conductivity of the entire bilayer system consisting of 8YSZ + 20YSZ (labelled 20AP) or 8YSZ + 55YSZ (55AP) rather than just individual layers of 20YSZ and 55YSZ. While this means the measured values are not solely due to the 20YSZ and 55YSZ top layers, this decision was influenced by previous studies which revealed that monolayers with a higher yttria content (>12 wt%) exhibit reduced fracture toughness and increased brittleness, potentially leading to premature failure unless a 7-8YSZ buffer layer is deposited alongside [6,30]. Thus, the analysis of a single-layer 20YSZ or 55YSZ system would not be representative of actual service conditions. Even more importantly, in this work, we also sought to investigate the influence of thermal cycling fatigue on thermal conductivity. This involved subjecting the samples to 30 ± 5 and 100 ± 5 thermal cycles at 1100 °C with 50 min of soaking time and 10 min of forced cooling in a lift furnace, according to the procedure described in detail in our previous work [6]. The thermal conductivity of the cycled samples was then measured and compared with that of the corresponding samples in their as-sprayed condition. This allowed us to investigate possible sintering effects, even though a furnace cycling test is not totally representative of real conditions due to the lack of a thermal gradient, as expressed in other works [31]. Thermal conductivity measurements on thermally cycled samples would have been impossible if single-layer 20YSZ and 55YSZ coatings had been employed, because they would have delaminated after only a few cycles.

As the TBC samples were applied to a Hastelloy-X substrate with a NiCoCrAlY bond coat, the contribution of both the substrate and the bond coat to the total heat flux through the system needed filtering. Therefore, thermal diffusivity measurements were conducted on uncoated Hastelloy X and bare bond-coated samples so that values of thermal conductivity of these materials could be determined and accounted for in measurements with multilayered systems. Thermal conductivity was determined through other properties according to Eq. (1) [32]:

$$\lambda = \alpha \cdot \rho \cdot C_p \tag{1}$$

where λ is the thermal conductivity, α is the thermal diffusivity, ρ is the density and C_p is the specific heat capacity of the sample.

The measurement of thermal diffusivity and specific heat capacity were performed through Laser Flash Analysis (LFA) and Differential Scanning Calorimetry (DSC), respectively. A NETZSCH LFA447 Laser Flash Analysis machine was used. The properties were determined at 25 °C (room temperature) performing 10 shots per sample to have a significant statistic, with a cooling time of 60 s between the shots, given the considerable mass of the samples.

Two coupons with 25.4 mm diameter for each material and treatment condition were tested using custom sample holders of suitable dimensions: the coated side was polished in order to reduce the surface roughness down to a Ra value in the 3–5 μm range, which was needed to reduce the error in the LFA readings. A sprayed graphite layer was applied on both surfaces of the specimen to ensure optimal absorption of the laser from the laser source and emission towards the sensor. The curves resulting from LFA analysis were fitted with a heat-loss model (Eq. (2)) that accounts for the thermal dispersion during the testing time, where L is the thickness of the sample (or of the single layer intended for the analysis) and (0.5) represents the time it takes for the temperature on the rear face to reach half of its peak value [15].

$$\alpha = \frac{0.1388 \bullet L^2}{t(0.5)} \tag{2}$$

The thickness values of the layers were measured by image analysis on optical microscope micrographs acquired on the cross-section of control specimens. Data resulting from the two samples (average and standard deviation of the 10 shots) was elaborated in an average value with standard deviation for each of the tested materials; the standard deviation was calculated considering the error propagation theory [33].

The software used for analysis (NETZSCH LFA *Proteus*) is able to analyse multiple-layered system. In this case, each individual layer was considered to be independent of the others, and it was assumed that the properties were known for all the layers but one. Thus, by sequentially testing the uncoated substrate, the substrate + bond coat system, and the complete TBC system the properties of the unknown outer layer could be computed from the measurement results in all cases. Elaborations based Eq. (2) can be used to determine the t(0.5) for the known layers. The difference of time between the total value obtained in the measurement on the multi-layered system and the contributions associated to the known layers was attributed to the unknown layer and its interface resistance, and then its diffusivity was calculated.

A differential scanning calorimeter (DSC) was used to determine the specific heat (C_p) of the samples, according to Eq. (3) [34].

$$DSC = m \cdot C_p \cdot s \cdot HR \tag{3}$$

where *m* is the sample mass, *HR* is the heating rate in the DSC acquisition, and *s* is the instrument sensitivity. The DSC signal is the electric voltage recorded by the instrument, which is proportional to the difference between the voltage recorded by the thermocouples positioned on the specimen and the reference pans, respectively. A small amount of material (15–25 mg) was obtained from the samples and tested in a DSC214 Polyma (NETZSCH, Selb, Germany) according to the ASTM E-1269/DIN 51007 standard, to determine the value of C_p at a temperature of 25 °C.

The materials for the DSC analysis were obtained with different methods. The Hastelloy X substrate was cut using an Al_2O_3 abrasive blade. The NiCoCrAlY bond coat was separated from the substrate by bending the sample. Samples of the ceramic top coat were obtained by chiselling a portion of the material and converting it into a fine powder.

DSC tests explored a ± 5 °C range around target temperature (20–30 °C). The standard procedure required a scanning program consisting of:

- 10 min isothermal phase at Tmin-30 °C = −10 °C
- Heating phase @10 K/min up to Tmax+30 °C = 60 °C
- 10 min isothermal phase at Tmax+30 °C = 60 °C

This same thermal cycle was repeated on the samples and the standard material (a sapphire crystal). The true specific heat of the sample was then calculated by comparison between the curves acquired on the sample and the standard material according to Eq. (4), where *m* are masses of the measured sample and the standard, *V* are the signals acquired in the DSC acquisitions, the subscripts *cal* and *sam* identify measures on the calibration sample and the sample of interest, respectively, and *bl* stands for baseline correction.

$$c_{P,sam}(T) = \frac{m_{cal}}{m_{sam}} \bullet \frac{(V_{sam}(T) - V_{bl}(T))}{(V_{cal}(T) - V_{bl}(T))} \bullet c_{P,cal} \tag{4}$$

Two measurements were performed on different samples for each material, and the resulting values were processed as Cp values as a function of temperature to be input into the LFA analysis software. The density of the materials used was estimated considering the specific gravity of the dense bulk materials. In the case of the ceramic top coat, the bulk density was corrected by the measured coating porosity, which was determined through image analysis software (ImageJ – NIH, Bethesda, Maryland, USA).

2.4. Nanoindentation testing

Nanoindentation experiments were conducted on carefully selected defect-free areas of the cross-section of the 20YSZ layer. The experiments were carried out using a G200 Nanoindenter from KLA Corporation, fitted with a Berkovich tip. The Continuous Stiffness Measurement (CSM) [20] mode was employed at a constant strain rate of 0.05 s^{-1} to a maximum depth of 500 nm. Before testing, the same experimental conditions were applied to a certified fused quartz reference to calibrate the machine's frame stiffness and the tip area function according to the ISO 14577 standard. Data indicating low modulus and hardness were excluded, as they were related to cracks and porosity, after validation by SEM imaging of the indented area. Data for the 55YSZ layer and the 8YSZ coating obtained from the agglomerated and sintered powder had been measured in our previous work under identical conditions [6]. By comparing coatings obtained using powders from the same manufacturing process, namely agglomeration and sintering, the differences can be more confidently ascribed to the sole effect of the chemical composition.

2.5. Indentation fracture toughness measurements via pillar-splitting

Likewise, the indentation fracture toughness of 8YSZ, 20YSZ, and 55YSZ layers obtained from agglomerated and sintered powders was measured to identify differences mainly due to composition alone. To achieve this, the pillar-splitting technique was adopted [21,35]. This technique involves precise nanoindentation of pillars that are shaped through focused ion beam (FIB) micro-milling, until unstable crack propagation occurs. A total of 15 micro-pillars were fabricated on the polished cross-section of each sample, following the milling parameters used in our previous study [29].

The pillars were fabricated using a Helios Nanolab 600 FIB/SEM microscope (ThermoFisher Scientific), each with a diameter (D) of 4.5 μm and an aspect ratio h/D ≥ 1 (Fig. 1-B). The fabrication process consisted of a multi-step semiautomated FIB milling procedure. Initially, a coarse milling phase was performed at a current of 0.92 nA and an acceleration voltage of 30 kV, followed by a final multi-step polishing and edge sharpening phase at 93 pA and 30 kV. This precise method ensured the reproducibility and accuracy of the dimensions of the pillars, as outlined in the referenced study.

After fabrication, some pillars underwent FIB sectioning to accurately measure their diameter and taper angle and check for pre-existing cracks in the material (Fig. 1-C). The fracture toughness (K_{IC}) was then determined by measuring the splitting load (P_C) during nanoindentation: $K_{IC} = \gamma \bullet P_C / R^{3/2}$, where *R* is the radius of the pillar. The dimensionless coefficient γ was determined through cohesive zone finite element modeling (CZ-FEM) in previous studies [22], where its dependence on E/H, Poisson's ratio, and indenter geometry was established. In our study, using a Berkovich indenter, the material properties and corresponding E/H ratios were first determined. The γ values were then obtained by interpolating the data from the simulations reported in these previous studies, selecting the values corresponding to a Poisson's ratio of 0.25, as used in our case. Given the limited variability of γ within the tested E/H range, and the relatively weak dependence on Poisson's ratio, an average γ value was assigned for each material (determined from their average E/H value) to ensure consistency and reliability in the fracture toughness calculations [22].

The results for the 8YSZ and 55YSZ layers were averaged together with the measurements that we had obtained under identical conditions in our previous study [29], in order to improve the reliability of the overall average.

The experiments were performed using a Keysight G200 nanoindenter equipped with a calibrated Berkovich tip, following the ISO 14577 standard. The tests were conducted at a strain rate of 0.05 s^{-1} and continued until a pop-in event in the load-displacement curve indicated

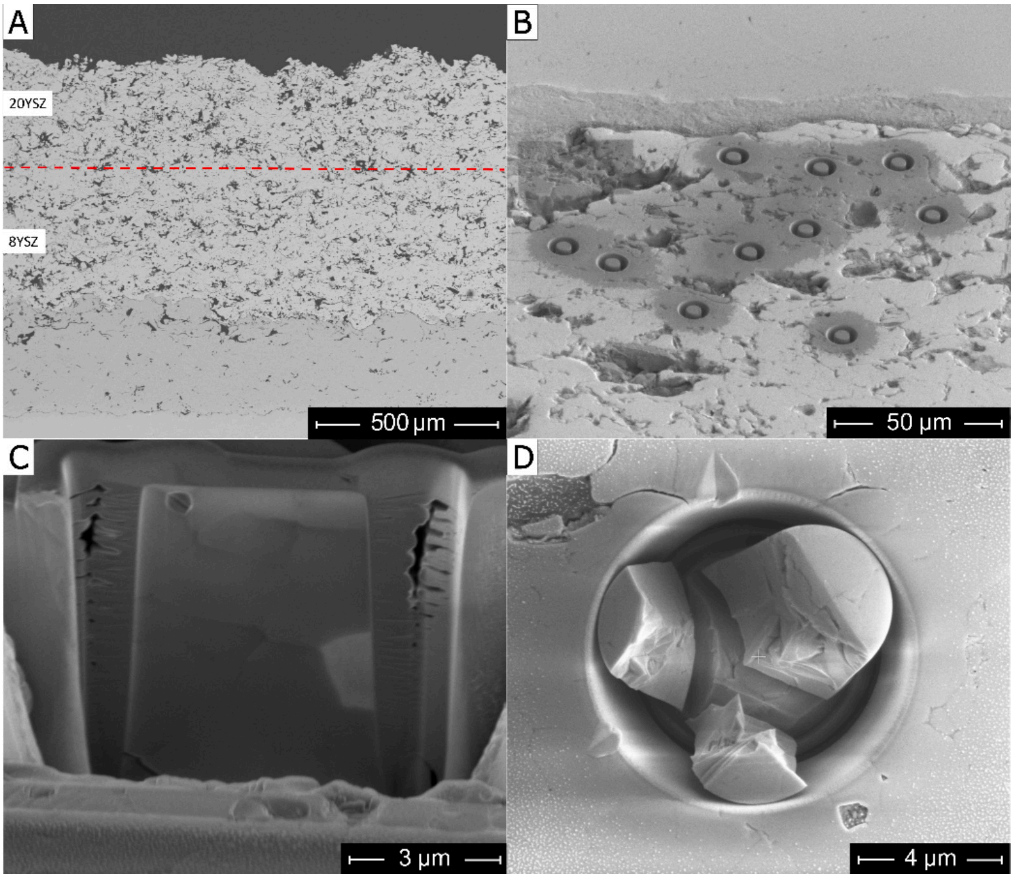

Fig. 1. A–B) 4.5 μm diameter pillars fabricated within the 20 wt% TBC layer; C) Focused Ion Beam (FIB) cross-sectioned micro-pillar for morphological and microstructural investigations (sub-superficial crack systems are visible); and D) a post-experiment image displaying a representative fractured pillar for a valid test.

pillar failure. To calculate the fracture toughness, at least six split pillars were analysed. Fig. 1-D illustrates an example of a post-splitting pillar. Images of each pillar were acquired and carefully examined to identify and exclude tip-pillar centre misalignments and abnormal cracking, such as non-3 fold-symmetric cracking.

3. Results and discussion

3.1. Monolayer 8YSZ coatings

3.1.1. Microstructures of powders and coatings

SEM micrographs of the three types of 8YSZ feedstock powders and the corresponding coatings (AP, FP and HP) are reported in Fig. 2. The use of powders with different morphologies produced coatings with different levels of porosity, as illustrated in Fig. 2(B, D, E). The porosity values obtained by image analysis (Fig. 3) are listed in Table 2, highlighting the distinction between globular porosity (Fig. 3-C) and microcracks (Fig. 3-D). The results indicate that the coating produced using the fused and crushed powder (FP) exhibited the lowest overall porosity. Specifically, it contained fewer globular pores and fewer microcracks compared to those deposited using A&S (AP) and HOSP powders (HP). The observed trend in porosity was as follows: AP > HP > FP. The variation in porosity of the as-sprayed samples can be attributed to the behaviour of the particles during the coating process. A&S particles, possessing a fine inner porosity (Fig. 2-A), had lower thermal conductivity and therefore melted with more difficulty than the fully dense F&C particles (Fig. 2-C). The retention of an unmelted core in the A&S particles also led to reduced droplet flattening upon impact and weaker bonding between particles, thus increasing the fraction of interlamellar microcracks. Kollenberg et al. also observed that coatings produced from agglomerated and sintered powders exhibited higher porosity compared to coatings produced from dense powders [36]. The HP coating contained fewer globular pores than the AP coating, because the dense, thin shell of the HOSP powder (Fig. 2-E) melted more effectively than the porous A&S aggregates. However, some of the inner pores of the HOSP particles, not all of which consisted of a thin shell with a large central void, could have been retained, and moreover, because the thin-shelled HOSP particles had a lower overall mass than F&C or A&S particles of similar size (most of their volume being occupied by the central void), they resulted in smaller, thinner lamellae. Thus, the HP coating, having the same thickness as the AP and FP coatings, contained a greater number of lamellae, increasing the chance of having interlamellar and intralamellar microcracks. Consequently, the HP coating had a content of microcracks similar to that of the AP coating (Table 2).

During thermal cycling, the smallest rounded voids and fine microcracks underwent sintering. This was visible in SEM micrographs acquired at high magnification after thermal fatigue cycling (Fig. 4), where some small pores disappeared and necks (see red arrows) formed between the opposing faces of the microcracks, sometimes leading to their conversion into arrays of nanometric rounded pores. The sintering phenomenon was already clearly visible after 30 cycles, with a corresponding decrease of the amounts of both globular porosity and microcracks in all coatings (Table 2). Interestingly, after 100 cycles the overall porosity of the FP and, more markedly, the HP coatings increased again. This may be attributed to the stiffening of the coatings caused by the initial sintering, which magnified the stresses induced by thermal cycling and caused the creation of new cracks and defects in the coating [12]. This corresponded to the initial stages of thermal cycling degradation of thermal barrier coatings as we showed previously in [37].

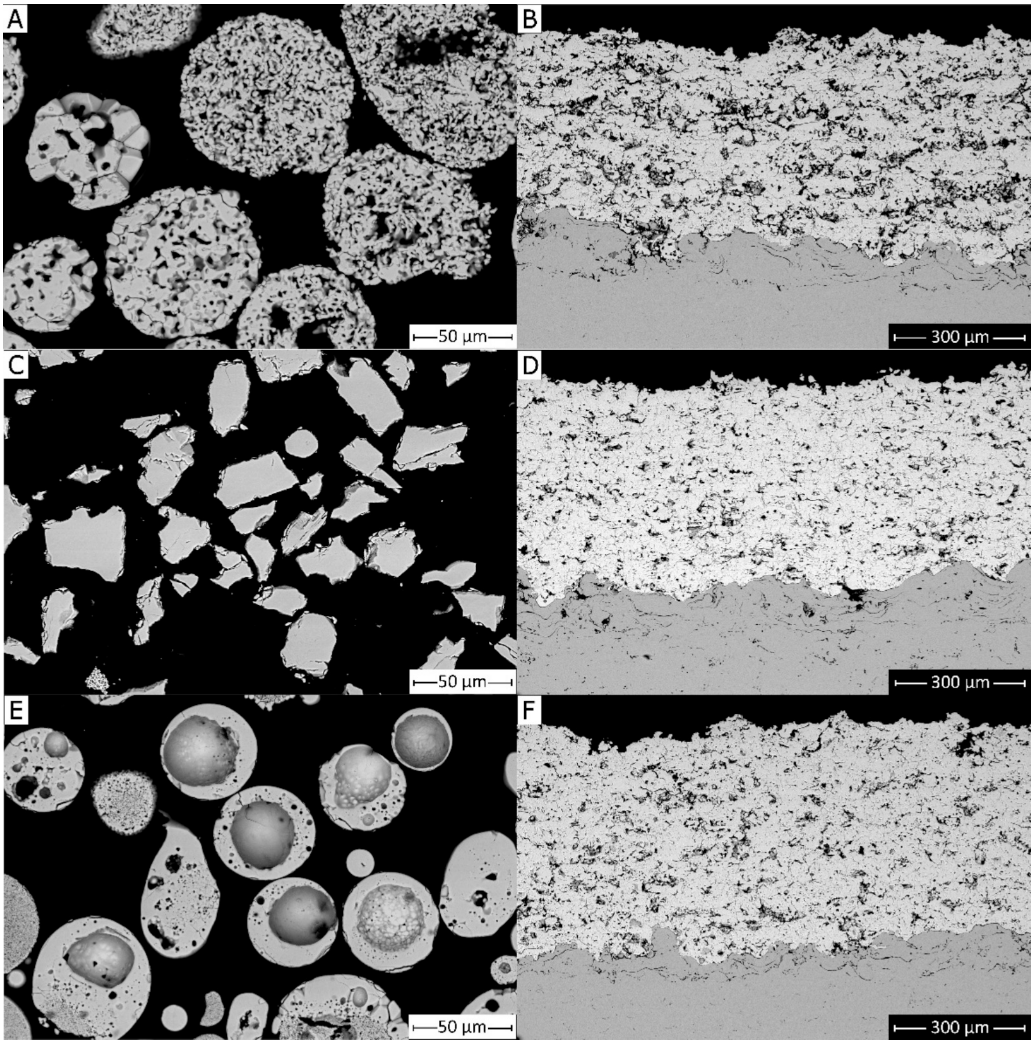

Fig. 2. BSE-SEM cross-sectional micrographs of the 8YSZ powders and the corresponding coatings: A) agglomerated and sintered (A&S), C) fused and crushed (F&C), and E) hollow spherical (HOSP) powders; B) AP, D) FP, and F) HP coatings.

3.1.2. Thermal diffusivity and conductivity results

The DSC curves, processed using the methods described in ASTM E-1269/DIN 51007, are presented in Fig. 5 within the temperature range of 20–30 °C. The values within this range were considered constant for the subsequent calculation of thermal conductivity. Therefore, a single specific heat value was obtained along with its standard deviation by aggregating all values in the measurement range. These specific heat values of all 8YSZ samples fell between 0.4 and 0.55 J/(g·K), as shown in Fig. 5, with the lowest value observed for the coating obtained from the HOSP powder (HP). Coatings obtained from A&S (AP) and F&C (FP) powders exhibited similar, higher values. The measured specific heat values were consistent with literature references for a standard YSZ TBC [38,39]. Notably, NiCoCrAlY (BC) showed a higher specific heat than the other materials (Fig. 5).

Estimates for the density of coating materials were obtained by considering the specific gravity of dense bulk materials. The assumption was made that the densities of thermally sprayed and bulk materials differed only due to porosity.

The theoretical density (ρth) of the bulk materials was set at 8.22 g/cm^3 for Hastelloy-X [40], 7.11 g/cm^3 for the NiCoCrAlY bond coat, and 6.4 g/cm^3 for 7-8YSZ. The computed density values (ρ) of the coatings, calculated based on their total porosity values, are shown in Table 3. The porosity of the bond coat was estimated to be in the range of 7–10 %. It was measured through Image Analysis of 5 optical micrographs acquired at 100×. Porosity and density values of the 8YSZ top coats were measured and calculated after 0, 30, and 100 thermal cycles, as reported in Tables 2 and 3, respectively. This assessment aimed to clarify the impact of thermal cycling on the thermal conductivity of the coatings.

Notably, the thermal conductivity of the Hastelloy X substrate (Table 3) was $\lambda \approx 10$ W/(m·K), which is consistent with the literature [41] and testifies to the reliability of the present measurements. The general trend of the thermal conductivity values of the 8YSZ coatings reflected the one observed in the thermal diffusivity (Table 3), since there were only small differences in density and specific heat values between the three coatings.

The relative trends among the different top coats in terms of thermal conductivity were in reasonable agreement with their porosity values. The AP coating showed the lowest thermal diffusivity and conductivity values in both the as-sprayed and thermally cycled conditions, compared to the FP and HP coatings (Table 3). This was consistent with its generally higher porosity (Table 2). Sintering after the initial 30 thermal fatigue cycles increased thermal diffusivity and conductivity in all cases. For the FP and HP coatings, after 30 ± 5 cycles, the thermal diffusivity and conductivity were more than doubled. On the other hand, the AP coating showed a lower increase in thermal diffusivity and conductivity after 30 ± 5 thermal cycles. Consistent with the general trends in porosity, the thermal diffusivity and conductivity values did not grow further after 100 ± 5 cycles.

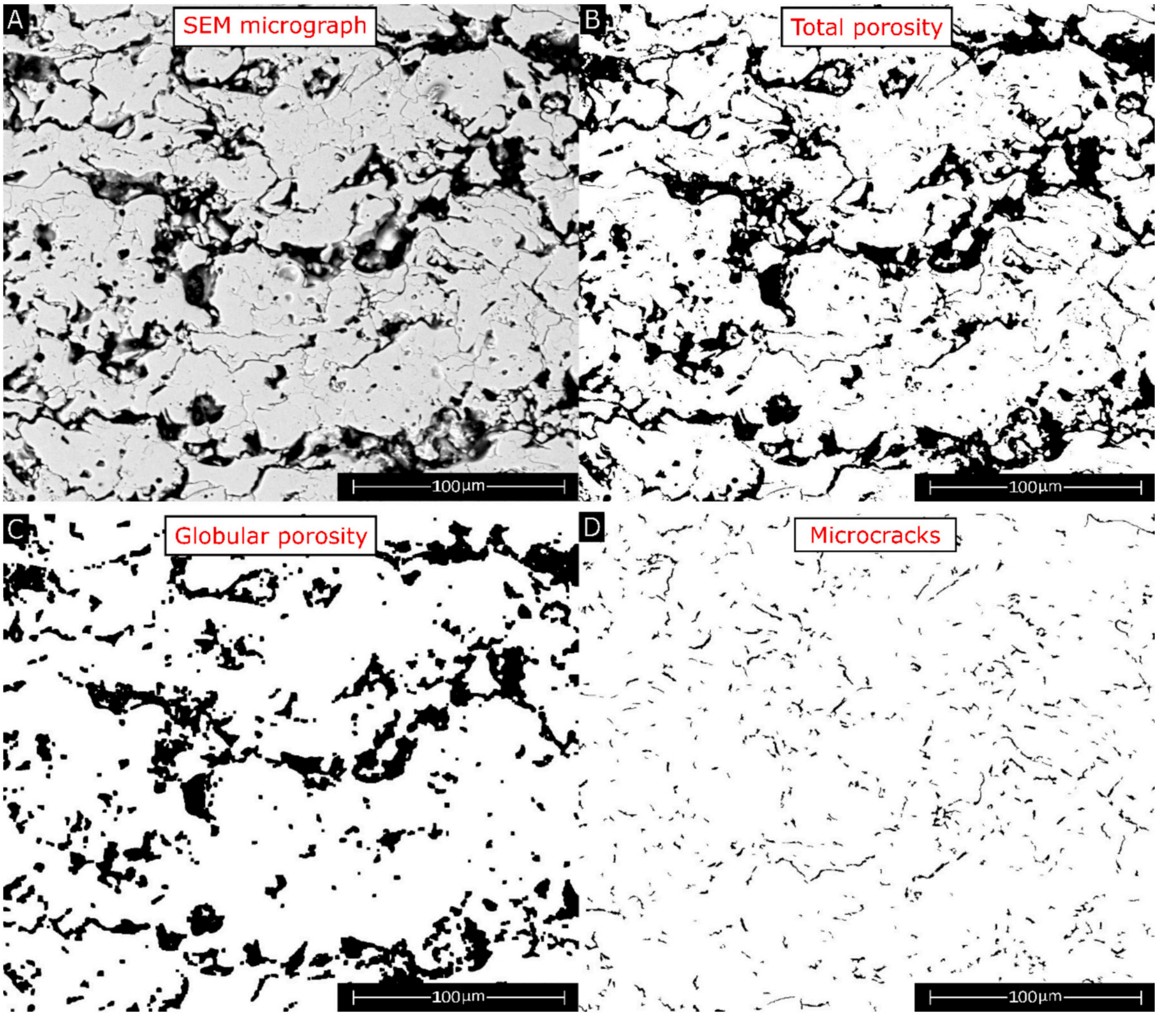

Fig. 3. Evaluation of porosity using image analysis, showcasing the different types of porosity present in the coatings. A) BSE-SEM micrograph, B) total porosity, C) globular porosity, and D) microcracks.

Table 2

Porosity values of monolayer samples in the as-deposited condition and after 30 and 100 thermal fatigue cycles.

Sample	Globular porosity [%]	Microcracks [%]	Total porosity [%]
AP as-deposited	18.5 ± 2.3	3.8 ± 0.3	22.3 ± 2.3
FP as-deposited	9.1 ± 1.5	2.7 ± 0.2	11.7 ± 1.6
HP as-deposited	12.5 ± 1.9	3.3 ± 0.1	15.7 ± 1.9
AP 30 cycles	16.4 ± 1.2	3.1 ± 0.3	19.5 ± 1.1
FP 30 cycles	6.9 ± 0.6	2.5 ± 0.2	9.5 ± 0.6
HP 30 cycles	12.4 ± 1.2	2.9 ± 0.4	15.3 ± 1.4
AP 100 cycles	15.0 ± 2.1	2.9 ± 0.4	17.9 ± 1.9
FP 100 cycles	8.3 ± 0.9	2.8 ± 0.3	11.1 ± 1.1
HP 100 cycles	15.6 ± 1.4	4.3 ± 0.4	19.9 ± 1.2

However, there were also some discrepancies between porosity (Table 2) and thermal diffusivity/conductivity values (Table 3). For example, the total porosity of the coatings increased significantly from 30 ± 5 to 100 ± 5 thermal fatigue cycles, but their thermal conductivity and diffusivity did not decrease by comparable amounts. The HP coating obtained from the HOSP powder even became more porous than the AP coating after 100 ± 5 cycles, but its thermal conductivity and diffusivity remained higher. There are various explanations for these discrepancies. First, image analysis cannot capture the finest pores and microcracks, which, however, did have a measurable effect on thermal conductivity. Second, not only the total amount, but also the shape, size, and orientation of pores influenced the thermal conductivity of a coating. Finally, due to the interaction between sintering and thermal shock during thermal fatigue cycling, it is possible that new cracks were opened in a coating where the original porosity became partly closed, meaning that the mounting resin might not have been able to infiltrate all of these newly formed cracks. The consequent pullouts may have resulted in an artificially higher porosity measured in the coatings after 100 ± 5 cycles by image analysis. Larger-sized pores and cracks remained unaffected by the sintering phenomenon observed after 30 and 100 cycles. Image analysis results indicate a slight increase in the percentage of interlamellar cracks after 100 cycles for the HP samples, while it remained the same for the AP and FP samples.

3.2. Bi-layered coatings

3.2.1. Microstructure, phase composition, and effect of yttria content on thermal properties

Fig. 6 illustrates that the agglomerated 20YSZ powder looked inhomogeneous, with coarse, bright particles among finer, darker ones. EDX spectra (Fig. 6-A) and maps (Fig. 6B–D) showed that the large, bright particles were rich in yttrium (spectrum 1 in Fig. 6-A), while the finest, darker particles (spectrum 2 in Fig. 6-A) were richer in zirconium. This suggests that the zirconia and yttria particles were mixed without undergoing significant sintering and interdiffusion. The lack of sintering of the powders caused the particles to melt non-uniformly during

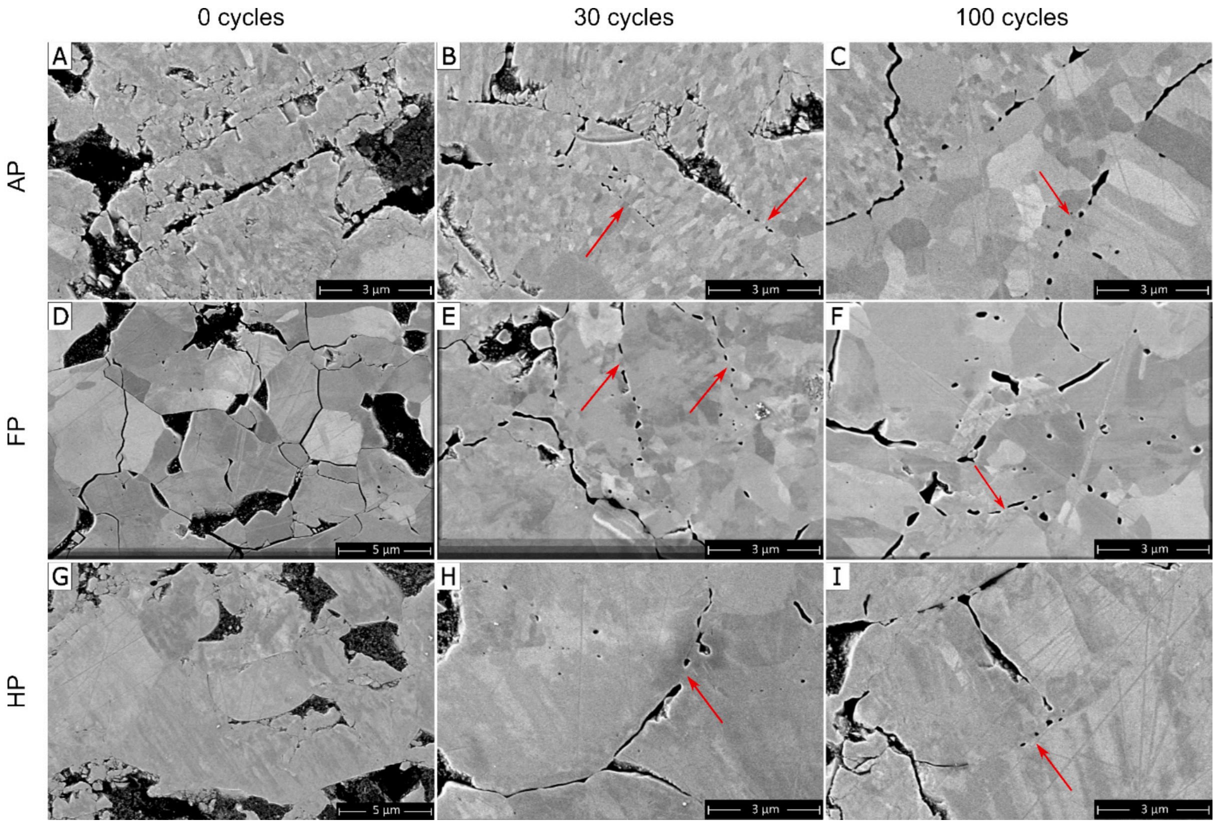

Fig. 4. BSE SEM micrographs of AP, FP, and HP samples in as-deposited condition (0 cycles) and after 30 and 100 thermal fatigue cycles. The red arrows indicate the closure of pores and microcracks due to sintering.

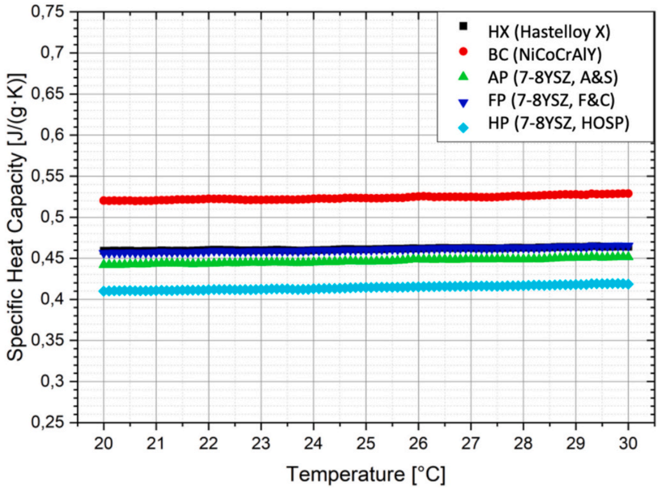

Fig. 5. Specific heat measurements for the HX (Hastelloy X), BC (bond coat, NiCoCrAlY), AP (agglomerated & sintered 8YSZ), FP (fused and crushed, 8YSZ) and HP (HOSP, 8YSZ) samples.

deposition, resulting in high interlamellar porosity and many microcracks between the splats (Fig. 7- red arrows), although, after spraying, the chemical inhomogeneity of the feedstock powder was no more identifiable and the coating had the expected 20YSZ overall composition.

Unlike the 20AP coating, the 55AP sample exhibited a higher density as shown in Table 4, primarily due to the denser 55YSZ top layer. Note, indeed, that the values in Table 4 refer to the whole bi-layer system made of the 20YSZ or 55YSZ top layer (respectively) and the 8YSZ bottom layer. This difference is mainly attributed to the lower porosity of the feedstock powders used, as indicated in Fig. 8. Moreover, the liquidus and solidus temperature of a 55YSZ system are slightly lower than those of 20YSZ [42,43], which might have helped the particles to melt better in the plasma jet.

The SEM micrograph of the 55AP coating is shown in Fig. 9. The coating contained a substantial amount of transverse microcracks across the splats (Fig. 9B). These were due to the well-known quenching stresses developed in solidified splats as they cooled and contracted very rapidly [44]. The fact that these microcracks seemed more abundant in the 55YSZ coating than in the 8YSZ was probably due to the lower fracture toughness of the 55YSZ composition, as will be shown in the next section, which made it even more sensitive to quenching-induced crack formation.

In the zirconia-yttria phase diagram, the proportions of the tetragonal and cubic high-temperature crystal structures of ZrO_2 that are retained at room temperature are influenced by the stabiliser content. When the yttria content exceeds 10 wt%, the low-temperature phase stabilises as cubic (C) [45]. The X-ray diffraction (XRD) patterns of monolayer and bilayer coatings obtained from the agglomerated and sintered powders of each composition (i.e. AP, 10AP and 55AP samples) are shown in Fig. 10. The monolayer AP coating, composed of a single 8YSZ layer, exhibited the characteristic peaks corresponding to the non-transformable tetragonal (t') zirconia phase. On the contrary, both the 20AP and 55AP samples showed XRD patterns indicative of cubic zirconia. Moreover, the diffraction peaks of the cubic phase shifted to lower diffraction angles (signifying an increasing lattice parameter) as the yttria content increased. Secondary peaks did not appear in the 20AP sample, consistent with the previous observation that the coating, unlike the feedstock powder, was chemically homogeneous, with no remaining separation between yttria-rich and yttria-lean areas.

The thermal conductivities of the bilayer systems are compared in

Table 3
Thermal diffusivity (α), density (ρ), specific heat (C_p) and thermal conductivity (λ) of the Hastelloy-X substrate, the NiCoCrAlY bond coat, and the AP (from the agglomerated & sintered 8YSZ powder), FP (from the fused and crushed 8YSZ powder) and HP (from the HOSP 8YSZ powder) coatings.

Samples	Thermal cycles	α [mm^2/s]	ρ [g/cm^3]	C_p [J/(g·K)]	λ [W/(m·K)]
Hastelloy-X	0	2.83 ± 0.14	8.22 ± 0.07	0.461 ± 0.002	10.73 ± 0.53
NiCoCrAlY	0	0.70 ± 0.05	6.51 ± 0.15	0.524 ± 0.003	2.38 ± 0.18
AP	0	0.26 ± 0.01	4.69 ± 0.20	0.457 ± 0.003	0.54 ± 0.02
	30	0.40 ± 0.01	4.89 ± 0.05		0.87 ± 0.02
	100	0.38 ± 0.01	4.96 ± 0.17		0.84 ± 0.03
FP	0	0.36 ± 0.01	5.34 ± 0.13	0.461 ± 0.003	0.89 ± 0.03
	30	0.95 ± 0.03	5.49 ± 0.05		2.39 ± 0.08
	100	0.99 ± 0.03	5.36 ± 0.10		2.44 ± 0.09
HP	0	0.33 ± 0.01	5.09 ± 0.16	0.414 ± 0.003	0.70 ± 0.02
	30	0.75 ± 0.02	5.11 ± 0.12		1.58 ± 0.05
	100	0.70 ± 0.02	4.84 ± 0.10		1.39 ± 0.04

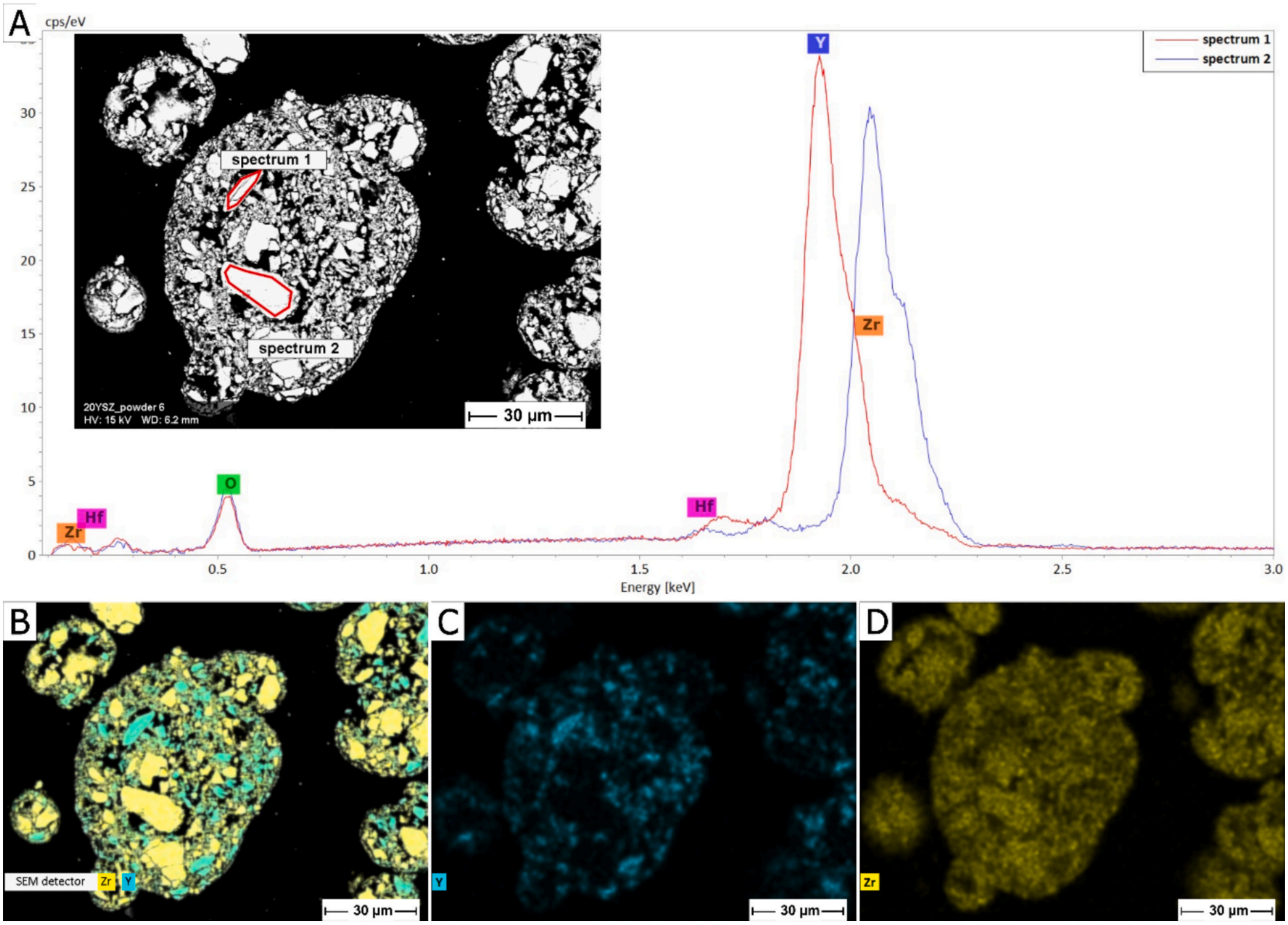

Fig. 6. (A) BSE-SEM micrograph and EDX spectra acquired on the cross-section of the 20YSZ powder; B) overall EDX map showing the distributions of Zr and Y; C) map of yttrium; D) map of zirconium.

Table 5. Although these values included contributions from both the 8YSZ bottom layer and the high-yttria top layers, the differences between the 20AP and 55AP samples and between them and the single-layer AP sample reflected the thermal properties of the top layer.

Hasselman established a distinct correlation between thermal conductivity and crystalline phase in zirconia ceramics: tetragonal zirconia demonstrates higher thermal conductivity than monoclinic zirconia, which, in turn, surpasses cubic zirconia in conductivity [1]. In this work, however, the relation is not as straightforward. In its as-sprayed state, the 20AP coating, with a cubic top layer, showed a slight reduction in thermal conductivity compared to the single-layer AP sample. However, despite its cubic phase, the 55AP sample exhibited higher thermal conductivity than the other samples. This means that microstructure played a more important role than chemical composition. The higher thermal conductivity of 55AP was due to the higher density of the entire coating system: ≈20 % porosity (Table 4) compared to the ≈22–23 % porosity of the single-layer AP samples (Table 2) and the bi-layer 20AP (Table 4) sample.

Notably, after thermal cycling fatigue tests, the porosity of the 55AP sample tended to decrease somewhat, while that of the 20AP sample was substantially unaffected (Table 4). Consistently, the thermal conductivity of the 55AP sample increased quite in same way as that of the

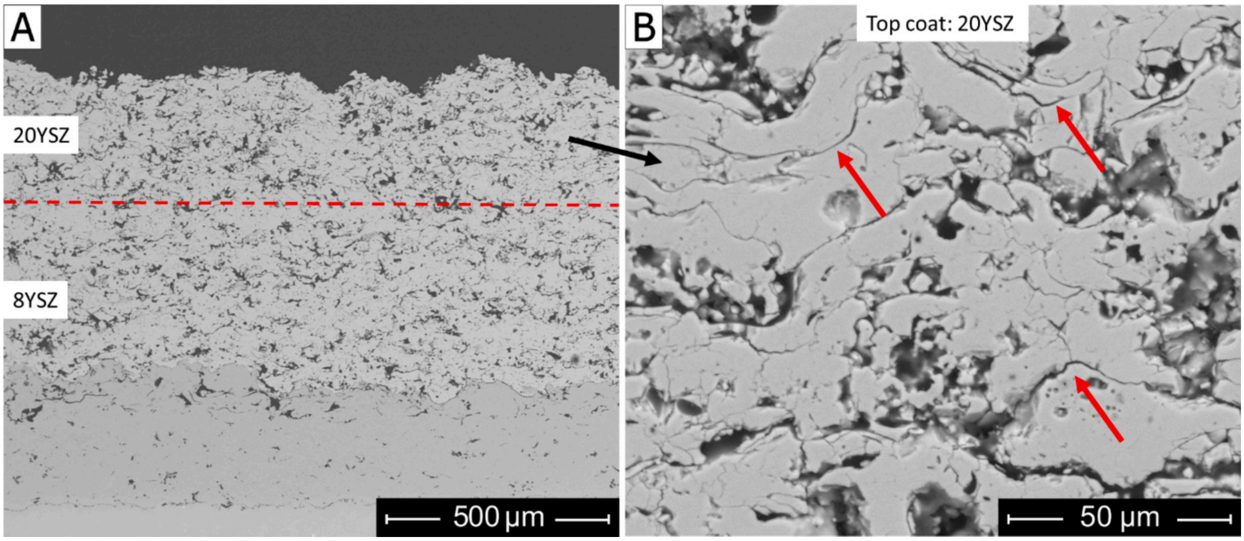

Fig. 7. BSE-SEM micrographs of the 20AP sample acquired at low (A) and high (B) magnification – the red arrows indicate interlamellar porosity.

Table 4
Porosity values of the bilayer coatings after different numbers of thermal fatigue cycles.

Sample	Total porosity [%]
20AP as-deposited	23.4 ± 3.2
20AP 30 cycles	23.1 ± 2.4
20AP 100 cycles	23.5 ± 3.1
55AP as-deposited	20.3 ± 2.6
55AP 30 cycles	19.8 ± 3.2
55AP 100 cycles	18.6 ± 4.1

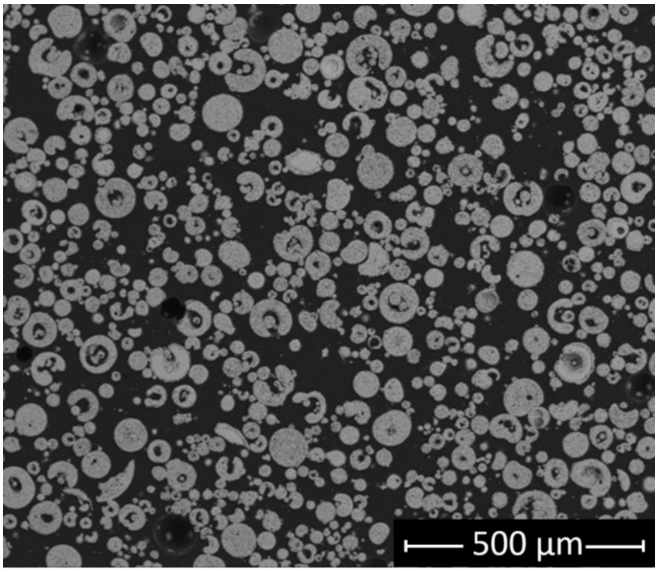

Fig. 8. BSE-SEM micrographs of 55YSZ agglomerated and sintered powder.

single-layer AP sample (Table 5), although it always retained values <1 W/(m•K), whereas the 20AP sample exhibited an almost insignificant increase in conductivity (Table 5). In both cases, there was no increase in porosity and no decrease in conductivity from 30 ± 5 to 100 ± 5 cycles, indicating that the sintering behaviour of the high-yttria compositions was different from that of 8YSZ.

3.2.2. Mechanical properties as a function of yttria content

As stated in the Introduction, this work also aimed to assess the mechanical properties associated with the incorporation of various amounts of yttria into zirconia. Specifically, we measured the small-scale mechanical properties of the 20YSZ top layer and compared them with the values we had previously measured on the 8YSZ and 55YSZ layers [29]. The depth-dependent properties obtained by nano-indentation measurements in the CSM mode (Fig. 11) and the values averaged in the 380 nm range (Table 6) highlighted a slight decrease in hardness and elastic modulus with increasing concentration of yttria, which was aligned with the literature findings [46,47].

Because hardness and elastic modulus did not decrease identically as a function of the increasing yttria content, the E/H ratio, which is an important indicator of a material's ability to deform elastically under loading, showed a nonlinear variation with the yttria content. At 20 wt% yttria, the lower E/H ratio suggests improved elastic deformation ability (lower elastic stiffness in proportion to the elastic deformation limit), which might in principle be beneficial to prevent inelastic failure of the material under loading (including under thermal fatigue cycling conditions) by limiting the accumulation of elastic stresses.

However, the ability of the material to limit the stress build-up should be accompanied by adequate toughness to enable the material to withstand such stress. That is, a material that is more elastically compliant but also significantly more brittle would likely not exhibit an improvement over a stiffer but substantially tougher material.

Indentation facture toughness measurements via micro-pillar splitting revealed that the 8YSZ layer exhibited the highest fracture toughness of 2.32 ± 0.40 MPa$\sqrt{m}$. On the contrary, both the 20 wt% Y_2O_3 layer and the 55 wt% Y_2O_3 layer exhibited average indentation values of approximately 1.39 MPa$\sqrt{m}$, with differences within the range of experimental uncertainty, indicating no statistically significant variation between the two compositions (Table 7). These results confirmed the inherent fracture toughness of the t' phase, known for its ferroelastic toughening mechanism. Because cubic zirconia lacks this toughening mechanism, a significant reduction in fracture toughness was produced as soon as the yttria content exceeded the threshold for the t' → c phase change. This transition and its impact on mechanical properties are well documented in the work of Yang et al. [48], which highlights the intrinsically lower toughness of the cubic phase. The present values were indeed quite consistent with those reported by Mercer et al. [3], who listed a fracture toughness of ≈3 MPa$\sqrt{m}$ for ZrO_2–7 wt% Y_2O_3 and ≈1.1 MPa$\sqrt{m}$ for ZrO_2–20 wt% Y_2O_3, although in our case the difference between the two compositions was slightly less marked.

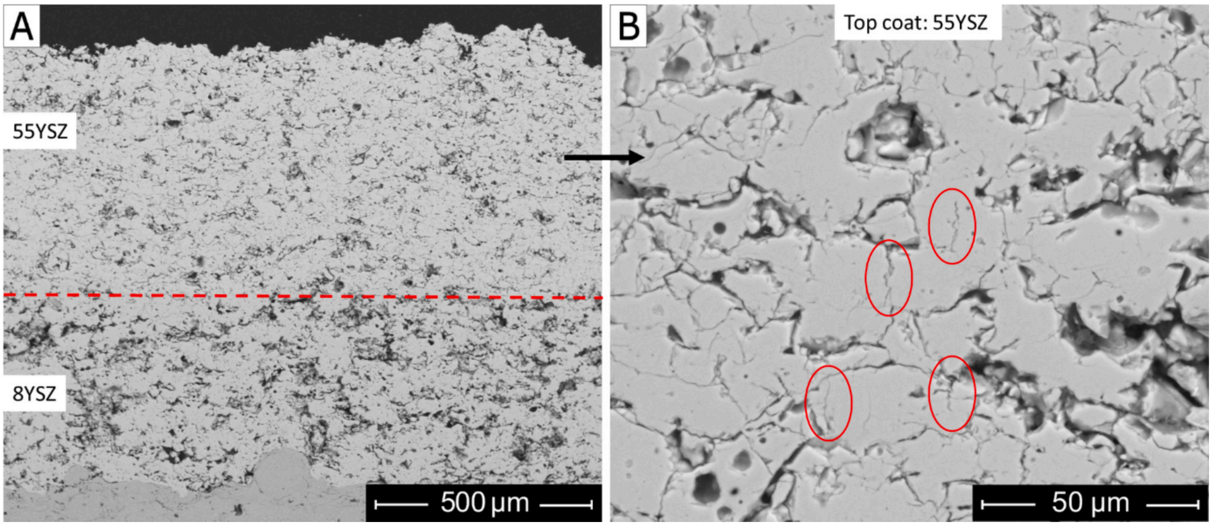

Fig. 9. BSE-SEM micrographs of the 55AP sample acquired at low (A) and high (B) magnifications – red circles indicate transverse microcracks.

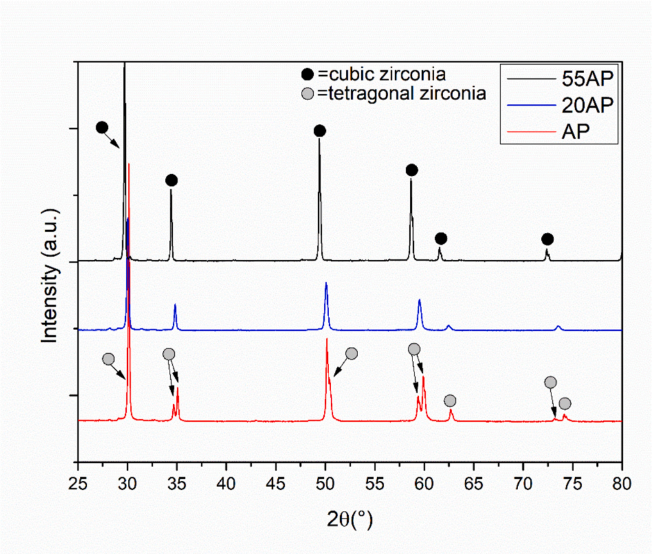

Fig. 10. XRD patterns of the AP, 20AP, and 55AP coatings.

Interestingly, fracture toughness seemed to be primarily dependent on phase composition: cubic zirconia with 20 wt% Y_2O_3 and 55 wt% Y_2O_3 exhibited identical toughness (Table 7).

The representative splitting curves, as showcased in Fig. 12, demonstrate the reliability and effectiveness of the pillar-splitting method in capturing these nuances. The observed pop-in events during the tests, combined with the gamma coefficient values derived from the elastic moduli obtained by CSM nanoindentations through finite element calibration curves, provided a comprehensive picture of the fracture toughness landscape in these coatings, also highlighting the higher scatter of the more porous 20YSZ and 8YSZ layers in comparison to the denser 55YSZ layer.

Pillar-splitting fracture toughness values inherently reflect the composite properties of the coatings, accounting for the porosity and other intrinsic microstructural features. Unlike methods that track crack propagation, pillar splitting provides a direct measure of the ultimate fracture toughness, integrating the effects of multiple mechanisms within the system. This makes it particularly well-suited for porous coatings, where defect interactions and pore distributions contribute to the overall fracture behaviour.

Observing the loading curves in Fig. 12, the 55 wt% Y_2O_3 loading curve presented a slightly steeper trend compared to 20 wt% Y_2O_3, although the 55 wt% Y_2O_3 and 20 wt% Y_2O_3 coatings exhibited similar elastic modulus (Table 6). This was consistent with the higher porosity of the 20 wt% Y_2O_3 coating, even if the bulk mechanical properties measured by nanoindentation in Table 6 were comparable. Therefore, consistent with the previous considerations, such differences in porosity could explain the higher scatter in the fracture toughness measurements for the 20YSZ coating, as local variations in density of the material within the pillar may have led to more pronounced fluctuations in the splitting loads.

4. Conclusions

- The manufacturing process and the resulting characteristics of the ZrO_2 – 8 wt% Y_2O_3 (8YSZ) feedstock powders had a measurable influence on the thermal diffusivity and conductivity of plasma-sprayed coatings. The finely distributed porosity of the agglomerated and sintered (A&S) powder resulted in coatings with higher overall porosity, including globular pores and elongated microcracks, which correspondingly exhibited lower thermal conductivity in the as-deposited condition (0.54 ± 0.02 W/(m·K)) compared to the coatings obtained with the hollow spherical (HOSP) powder

Table 5
Thermal diffusivity (α), density (ρ), specific heat (Cp), and thermal conductivity (λ) of the 20AP and 55AP bilayer systems after 0,30, and 100 thermal fatigue cycles.

Samples	Thermal cycles	α [mm^2/s]	ρ [g/cm^3]	C_p [J/(g·K)]	λ [W/(m·K)]
20AP	0	0.33 ± 0.01	3.89 ± 0.23	0.397 ± 0.033	0.51 ± 0.05
	30	0.39 ± 0.01	3.90 ± 0.17		0.60 ± 0.06
	100	0.39 ± 0.01	3.88 ± 0.22		0.61 ± 0.06
55AP	0	0.29 ± 0.01	4.64 ± 0.22	0.456 ± 0.002	0.61 ± 0.03
	30	0.35 ± 0.03	4.67 ± 0.26		0.75 ± 0.04
	100	0.44 ± 0.03	4.75 ± 0.34		0.95 ± 0.12

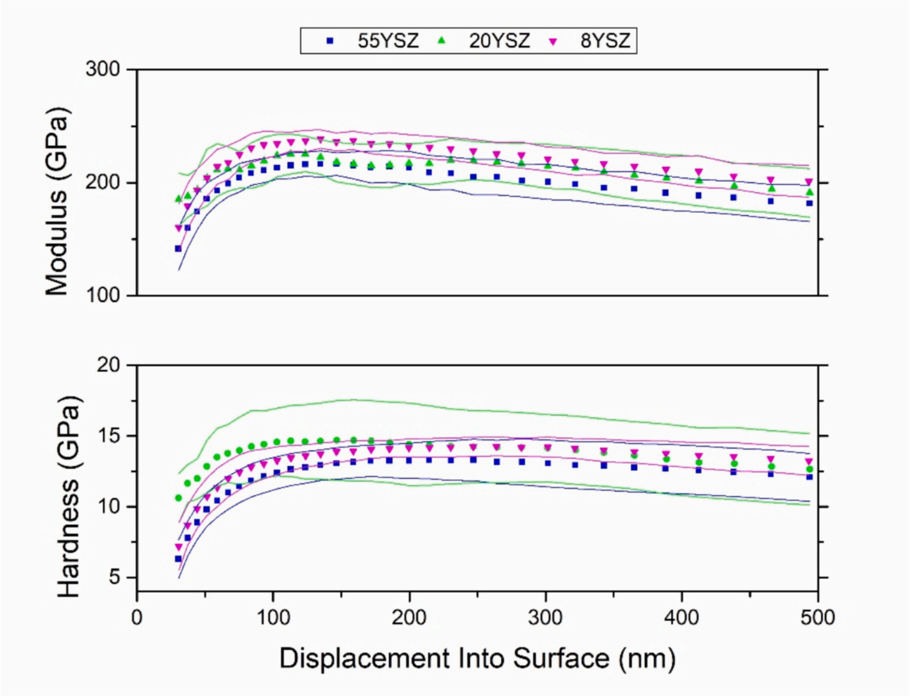

Fig. 11. Elastic modulus and hardness values from nanoindentation tests in Continuous Stiffness Measurement mode averaged across valid tests performed on homogeneous and defect-free areas of the 8YSZ bottom layer and the top layers of the 20YSZ and 55YSZ systems.

Table 6
Elastic modulus, hardness, and E/H ratio as a function of the weight percentage of yttria from Continuous Stiffness Measurement nanoindentation.

Yttria content (wt%)	Elastic modulus (GPa)	Hardness (GPa)	E/H
7–8	233 ± 10	14.2 ± 0.6	16.4 ± 1.4
20	216 ± 19	14.4 ± 2.9	14.9 ± 4.2
55	212 ± 14	13.3 ± 1.2	16.0 ± 2.6

Table 7
Critical loads (P_c), calibration coefficients, and fracture toughness values calculated from pillar splitting experiments as a function of the wt% of yttria.

Wt% yttria	P_c (mN)	γ (−)	K_c ($MPa\sqrt{m}$)
8YSZ	23.88 ± 4.17	0.327	2.32 ± 0.40
20YSZ	15.46 ± 5.95	0.304	1.39 ± 0.54
55YSZ	14.72 ± 1.58	0.320	1.398 ± 0.150

(0.70 ± 0.02 W/(m·K)) and the much denser ones obtained with the fused and crushed (F&C) powder (0.89 ± 0.03 W/(m·K)).

- The porosity of all 8YSZ coatings decreased after 30 ± 5 thermal fatigue cycles due to sintering, which reduced the overall content of both globular pores and elongated microcracks. Correspondingly, their thermal conductivity increased in all cases. However, the increase was much less marked in the coating obtained with the A&S powder (0.87 ± 0.02 W/(m·K)) compared to those obtained with HOSP (2.39 ± 0.08 W/(m·K)) and F&C powders (1.58 ± 0.05 W/(m·K)). After 100 ± 5 cycles, the porosity increased again due to thermal shock, and correspondingly, the thermal conductivity remained approximately constant or decreased slightly in all cases.
- The thermal conductivity values of the bi-layer coatings with an 8YSZ bottom layer and a ZrO_2 – 20 wt% Y_2O_3 (20YSZ) or ZrO_2 – 55 wt% Y_2O_3 (55YSZ) top layer were in the range of 0.51 W/(m·K) (20YSZ) and 0.61 W/(m·K) (55YSZ), respectively, and appeared to depend more on the porosity of the top coat than the Y_2O_3 content. After 30 ± 5 thermal fatigue cycles, the evolution in porosity and thermal conductivity of the bi-layer systems was similar to the 8YSZ single-layer coating, but there were no further changes after 100 ± 5 cycles, suggesting a different long-term evolution.

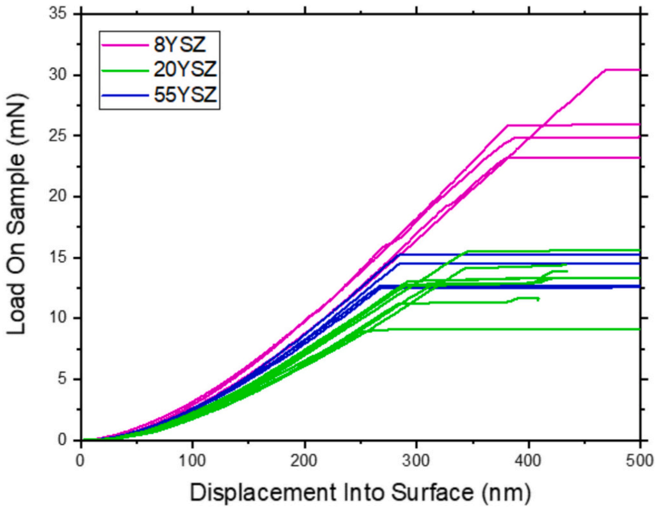

Fig. 12. Load On Sample versus Displacement Into Surface curves corresponding to representative micro-pillar splitting experiments performed on top coats with different compositions.

- There was a measurable difference between the indentation fracture toughness values of the 8YSZ coating, with a non-transformable tetragonal (t') structure, and the 20YSZ and 55YSZ coatings, fully stabilized in the cubic structure. The toughness of 8YSZ was 2.32 ± 0.40 MPa$\sqrt{m}$, while the 20YSZ and 55YSZ layers both exhibited toughness values of ≈1.39 MPa$\sqrt{m}$. Therefore, it appears that the fracture toughness of the fully stabilized zirconia compositions did not depend on the amount of Y_2O_3. It is finally remarked that these values, which were obtained by pillar-splitting on dense areas of the coating, were nonetheless partly dependent on the microstructure of the coating, because of the possible presence of sub-surface defects in the volume of the pillars.

CRediT authorship contribution statement

Stefania Morelli: Writing – review & editing, Methodology, Conceptualization, Writing – original draft, Investigation, Visualization, Formal analysis. **Simone Bursich:** Writing – original draft, Investigation, Visualization, Formal analysis, Writing – review & editing, Methodology, Conceptualization. **Giovanni Bolelli:** Supervision, Formal analysis, Writing – review & editing, Methodology, Conceptualization, Visualization, Investigation. **Pietro Puddu:** Writing – review & editing, Formal analysis, Methodology, Investigation. **Edoardo Rossi:** Methodology, Investigation, Writing – review & editing, Formal analysis. **Francesco Gerardo Mecca:** Investigation, Formal analysis, Methodology. **Luca Bortolotti:** Investigation, Formal analysis, Methodology. **Luca Lusvarghi:** Project administration, Writing – review & editing, Conceptualization, Supervision.

Declaration of competing interest

The authors declare that they have no known competing financial interests or personal relationships that could have appeared to influence the work reported in this paper.

Data availability

Data will be made available on request.

References

[1] D.P.H. Hasselman, L.F. Johnson, L.D. Bentsen, R. Syed, H.L. Lee, M.V. Swain, Thermal diffusivity and conductivity of dense polycrystalline ZrO_2 ceramics: a survey, Am. Ceram. Soc. Bull. 66 (1987) 799–806.

[2] X. Song, Y. Ding, J. Zhang, C. Jiang, Z. Liu, C. Lin, W. Zheng, Y. Zeng, Thermophysical and mechanical properties of cubic, tetragonal and monoclinic ZrO2, J. Mater. Res. Technol. 23 (2023) 648–655, https://doi.org/10.1016/J.JMRT.2023.01.040.

[3] C. Mercer, J.R. Williams, D.R. Clarke, A.G. Evans, On a ferroelastic mechanism governing the toughness of metastable tetragonal-prime (t′) yttria-stabilized zirconia, Proc. R. Soc. A: Math. Phys. Eng. Sci. 463 (2007) 1393–1408, https://doi.org/10.1098/rspa.2007.1829.

[4] R. Taylor, J.R. Brandon, P. Morrell, Microstructure, composition and property relationships of plasma-sprayed thermal barrier coatings, Surf. Coat. Technol. 50 (1992) 141–149, https://doi.org/10.1016/0257-8972(92)90055-F.

[5] H. Memon, A.R. Romero, S. Lokachari, Z. Xu, X. Wang, K. Leng, N. Curry, M. Li, T. Hussain, Influence of yttria content in YSZ: an evaluation of water-based SPS coatings and spark plasma sintered pellets, Surf. Coat. Technol. 488 (2024) 131046, https://doi.org/10.1016/J.SURFCOAT.2024.131046.

[6] S. Bursich, S. Morelli, G. Bolelli, G. Cavazzini, E. Rossi, F.G. Mecca, S. Petruzzi, E. Bemporad, L. Lusvarghi, The effect of ceramic YSZ powder morphology on coating performance for industrial TBCs, Surf. Coat. Technol. 476 (2024) 130270, https://doi.org/10.1016/J.SURFCOAT.2023.130270.

[7] S.V. Shinde, E.J. Gildersleeve, C.A. Johnson, S. Sampath, Segmentation crack formation dynamics during air plasma spraying of zirconia, Acta Mater. 183 (2020) 196–206, https://doi.org/10.1016/j.actamat.2019.10.052.

[8] D.R. Clarke, C.G. Levi, Materials design for the next generation thermal barrier coatings, Annu. Rev. Mat. Res. 33 (2003) 383–417, https://doi.org/10.1146/annurev.matsci.33.011403.113718.

[9] G. Bertrand, P. Bertrand, P. Roy, C. Rio, R. Mevrel, Low conductivity plasma sprayed thermal barrier coating using hollow psz spheres: correlation between thermophysical properties and microstructure, Surf. Coat. Technol. 202 (2008) 1994–2001, https://doi.org/10.1016/j.surfcoat.2007.08.042.

[10] A. Kulkarni, Z. Wang, T. Nakamura, S. Sampath, A. Goland, H. Herman, J. Allen, J. Ilavsky, G. Long, J. Frahm, R.W. Steinbrech, Comprehensive microstructural characterization and predictive property modeling of plasma-sprayed zirconia coatings, Acta Mater. 51 (2003) 2457–2475, https://doi.org/10.1016/S1359-6454(03)00030-2.

[11] W. Chi, S. Sampath, H. Wang, Ambient and high-temperature thermal conductivity of thermal sprayed coatings, Proc. Int. Therm. Spray Conf. 15 (2006) 773–778, https://doi.org/10.1361/105996306X146730.

[12] N. Markocsan, P. Nylén, J. Wigren, X.H. Li, A. Tricoire, Effect of thermal aging on microstructure and functional properties of zirconia-base thermal barrier coatings, J. Therm. Spray Technol. 18 (2009) 201–208, https://doi.org/10.1007/s11666-009-9313-6.

[13] Y. Huang, N. Hu, Y. Zeng, X. Song, C. Lin, Z. Liu, J. Zhang, Effect of different types of pores on thermal conductivity of YSZ thermal barrier coatings, Coatings 9 (2019) 1–10, https://doi.org/10.3390/COATINGS9020138.

[14] L. Pawlowski, P. Fauchais, Thermal transport properties of thermally sprayed coatings, Int. Mater. Rev. 37 (1992) 271–289, https://doi.org/10.1179/imr.1992.37.1.271.

[15] R.E. Taylor, Thermal conductivity determinations of thermal barrier coatings, Mater. Sci. Eng. A 245 (1998) 160–167, https://doi.org/10.1016/S0921-5093(97)00847-2.

[16] K. Kim, W. Kim, Effect of heat treatment on microstructure and thermal conductivity of thermal barrier coating, Materials 14 (2021), https://doi.org/10.3390/ma14247801.

[17] H. Zhang, Y. Chen, L. Li, D. Yang, X. Liu, A. Huang, X. Zhang, J. Lu, X. Zhao, Unraveling the CMAS corrosion mechanism of APS high-yttria-stabilized zirconia thermal barrier coatings, J. Eur. Ceram. Soc. 44 (2024) 5154–5165, https://doi.org/10.1016/J.JEURCERAMSOC.2024.02.032.

[18] W. Li, H. Zhao, X. Zhong, L. Wang, S. Tao, Air plasma-sprayed yttria and yttria-stabilized zirconia thermal barrier coatings subjected to calcium-magnesium-alumino-silicate (CMAS), J. Therm. Spray Technol. 23 (2014) 975–983, https://doi.org/10.1007/s11666-014-0107-0.

[19] W.C. Oliver, G.M. Pharr, Measurement of hardness and elastic modulus by instrumented indentation: advances in understanding and refinements to methodology, J. Mater. Res. 19 (2004) 3–20, https://doi.org/10.1557/jmr.2004.19.1.3.

[20] W.C. Oliver, G.M. Pharr, An improved technique for determining hardness and elastic modulus using load and displacement sensing indentation experiments, J. Mater. Res. 7 (1992) 1564–1583, https://doi.org/10.1557/JMR.1992.1564.

[21] M. Sebastiani, K.E. Johanns, E.G. Herbert, F. Carassiti, G.M. Pharr, A novel pillar indentation splitting test for measuring fracture toughness of thin ceramic coatings, Philos. Mag. 95 (2015) 1928–1944, https://doi.org/10.1080/14786435.2014.913110.

[22] M. Ghidelli, M. Sebastiani, K.E. Johanns, G.M. Pharr, Effects of indenter angle on micro-scale fracture toughness measurement by pillar splitting, J. Am. Ceram. Soc. 100 (2017) 5731–5738, https://doi.org/10.1111/jace.15093.

[23] J.F. Nonemacher, Y. Arinicheva, G. Yan, M. Finsterbusch, M. Krüger, J. Malzbender, Fracture toughness of single grains and polycrystalline Li7La3Zr2O12 electrolyte material based on a pillar splitting method, J. Eur. Ceram. Soc. 40 (2020) 3057–3064, https://doi.org/10.1016/j.jeurceramsoc.2020.03.028.

[24] M. Sebastiani, K.E. Johanns, E.G. Herbert, G.M. Pharr, Measurement of fracture toughness by nanoindentation methods: recent advances and future challenges, Curr. Opin. Solid State Mater. Sci. 19 (2015) 324–333, https://doi.org/10.1016/j.cossms.2015.04.003.

[25] G.K. Beshish, C.W. Florey, F.J. Worzala, W.J. Lenling, Fracture toughness of thermal spray ceramic coatings determined by the indentation technique, J. Therm. Spray Technol. 2 (1993) 35–38, https://doi.org/10.1007/BF02647421.

[26] E. Salvati, T. Sui, A.J.G. Lunt, A.M. Korsunsky, The effect of eigenstrain induced by ion beam damage on the apparent strain relief in FIB-DIC residual stress evaluation, Mater. Des. 92 (2016) 649–658, https://doi.org/10.1016/j.matdes.2015.12.015.

[27] M. Renzelli, M.Z. Mughal, M. Sebastiani, E. Bemporad, Design, fabrication and characterization of multilayer Cr-CrN thin coatings with tailored residual stress profiles, Mater. Des. 112 (2016) 162–171, https://doi.org/10.1016/j.matdes.2016.09.058.

[28] G. Bolelli, M.G. Righi, M.Z. Mughal, R. Moscatelli, O. Ligabue, N. Antolotti, M. Sebastiani, L. Lusvarghi, E. Bemporad, Damage progression in thermal barrier coating systems during thermal cycling: a nano-mechanical assessment, Mater. Des. 166 (2019) 107615, https://doi.org/10.1016/j.matdes.2019.107615.

[29] S. Bursich, S. Morelli, G. Bolelli, G. Cavazzini, E. Rossi, F.G. Mecca, S. Petruzzi, E. Bemporad, L. Lusvarghi, The effect of ceramic YSZ powder morphology on coating performance for industrial TBCs, Surf. Coat. Technol. 476 (2024) 130270, https://doi.org/10.1016/j.surfcoat.2023.130270.

[30] V. Viswanathan, G. Dwivedi, S. Sampath, Multilayer, multimaterial thermal barrier coating systems: design, synthesis, and performance assessment, J. Am. Ceram. Soc. 98 (2015) 1769–1777, https://doi.org/10.1111/jace.13563.

[31] N. Curry, J. Donoghue, Evolution of thermal conductivity of dysprosia stabilised thermal barrier coating systems during heat treatment, Surf. Coat. Technol. 209 (2012) 38–43, https://doi.org/10.1016/j.surfcoat.2012.08.018.

[32] N. Curry, N. Markocsan, X.H. Li, A. Tricoire, M. Dorfman, Next generation thermal barrier coatings for the gas turbine industry, J. Therm. Spray Technol. 20 (2011) 108–115, https://doi.org/10.1007/s11666-010-9593-x.

[33] B. Lin, C. Li, C. Su, H. Ban, R.N. Scripa, S.L. Lehoczky, Method for obtaining thermal conductivity from modified laser flash measurement, in: American Society of Mechanical Engineers, Heat Transfer Division, 2005, pp. 725–730, https://doi.org/10.1115/IMECE2005-79932.

[34] M. Reading, D.J. Hourston (Eds.), Modulated Temperature Differential Scanning Calorimetry, Springer Netherlands, Dordrecht, 2006, https://doi.org/10.1007/1-4020-3750-3.

[35] C.M. Lauener, L. Petho, M. Chen, Y. Xiao, J. Michler, J.M. Wheeler, Fracture of silicon: influence of rate, positioning accuracy, FIB machining, and elevated temperatures on toughness measured by pillar indentation splitting, Mater. Des. 142 (2018) 340–349, https://doi.org/10.1016/j.matdes.2018.01.015.

[36] W. Kollenberg, J. Decker, Influence of powder-characteristics on the microstructure of ceramic plasma spray coatings, Fresenius J. Anal. Chem. 346 (1993) 327–333, https://doi.org/10.1007/BF00321444.

[37] G. Bolelli, M.G. Righi, M.Z. Mughal, R. Moscatelli, O. Ligabue, N. Antolotti, M. Sebastiani, L. Lusvarghi, E. Bemporad, Damage progression in thermal barrier coating systems during thermal cycling: a nano-mechanical assessment, Mater. Des. 166 (2019) 107615, https://doi.org/10.1016/j.matdes.2019.107615.

[38] Y. Wang, W. Wu, X. Zheng, Y. Zeng, M. Ding, C. Zhang, Relationship between the microstructure and thermal conductivity of plasma-sprayed ZrO 2 coatings, J. Therm. Spray Technol. 20 (2011) 1177–1182, https://doi.org/10.1007/s11666-011-9660-y.

[39] J. Wu, H.B. Guo, L. Zhou, L. Wang, S.K. Gong, Microstructure and thermal properties of plasma sprayed thermal barrier coatings from nanostructured YSZ, J. Therm. Spray Technol. 19 (2010) 1186–1194, https://doi.org/10.1007/s11666-010-9535-7.

[40] HASTELLOY® X - Haynes International. n.d.. https://haynesintl.com/en/alloys/alloy-portfolio/high-temperature-alloys/hastelloy-x/ (accessed January 19, 2025).

[41] S. Ulan kyzy, R. Völkl, O. Munz, T. Fischer, S. Welzenbach, U. Glatzel, Thermo-physical properties of Hastelloy X and Haynes 214 close to the melting range, Mater. Sci. Technol. 36 (2020) 1012–1019, https://doi.org/10.1080/02670836.2020.1753154.

[42] L. Li, O. Van Der Biest, P.L. Wang, J. Vleugels, W.W. Chen, S.G. Huang, Estimation of the phase diagram for the ZrO2–Y2O3–CeO2 system, J. Eur. Ceram. Soc. 21 (2001) 2903–2910, https://doi.org/10.1016/S0955-2219(01)00218-7.

[43] O. Fabrichnaya, F. Aldinger, Assessment of thermodynamic parameters in the system ZrO2–Y2O3–Al2O3, Int. J. Mater. Res. 95 (2004) 27–39, https://doi.org/10.3139/IJMR-2004-0007.

[44] S. Kuroda, T.W. Clyne, The quenching stress in thermally sprayed coatings, Thin Solid Films 200 (1991) 49–66, https://doi.org/10.1016/0040-6090(91)90029-W.

[45] J.R. Nicholls, K.J. Lawson, A. Johnstone, D.S. Rickerby, Methods to reduce the thermal conductivity of EB-PVD TBCs, Surf. Coat. Technol. 151 (2002) 383–391, https://doi.org/10.1016/S0257-8972(01)01651-6.

[46] A. Kumar, J. Moledina, Y. Liu, K. Chen, P.C. Patnaik, Nano-micro-structured 6%–8% YSZ thermal barrier coatings: a comprehensive review of comparative performance analysis, Coatings 11 (2021) 239–262, https://doi.org/10.3390/coatings11121474.

[47] B. Vignesh, W.C. Oliver, G.S. Kumar, P.S. Phani, Critical assessment of high speed nanoindentation mapping technique and data deconvolution on thermal barrier coatings, Mater. Des. 181 (2019) 108084, https://doi.org/10.1016/j.matdes.2019.108084.

[48] G.J. Yang, Z.L. Chen, C.X. Li, C.J. Li, Microstructural and mechanical property evolutions of plasma-sprayed YSZ coating during high-temperature exposure: comparison study between 8YSZ and 20YSZ, J. Therm. Spray Technol. 22 (2013) 1294–1302, https://doi.org/10.1007/s11666-013-9986-8.